Quantitative Evaluation of Mass Transfer near the Edge of Porous Media by Absorption Photometry

Taiki Tanikoshi

Faculty of Engineering, Hokkaido University, N13-W8, Sapporo, 0608628, Japan

Ryoko Otomo

Faculty of Engineering Science, Kansai University, 3-3-35, Yamate-cho, Suita, 5648680, Japan

Shusaku Harada

Faculty of Engineering, Hokkaido University, N13-W8, Sapporo, 0608628, Japan

Correspondence : otomo@kansai-u.ac.jp

This paper reports the intensive investigation of mass transfer near the entrance (edge) of porous media by quantification of the surrounding concentration field. We have adopted a non-invasive and real-time system based on light absorption photometry for measurement of the concentration field in a quasi-two dimensional cell. This system is, in principle, applicable to the measurement of various substances due to the generality of light absorption. This measurement system was applied to a simple model of the gravity-driven transport of a substance in a fluid near the edge of a porous medium in the presence of a reaction at the surface. The temporal variation of the complicated concentration field is appropriately captured with a spatial resolution of several tens of micrometers to millimeters. Quantitative analyses revealed that the geometry of the porous edge considerably affects the convection flow and invasion of substances into the medium.

Keywords: Porous Media, Light Absorption Photometry, Convection Flow, Solid-Liquid Interface, Rayleigh-Taylor Instability

Introduction

Knowledge of the mechanisms of mass transfer in porous media provides valuable insights in various engineering processes, such as separation and purification in chemical engineering, catalytic reactions in mechanical engineering, contamination control in soils and rocks in environmental engineering[1], and gas and oil exploration in resource engineering[2]. One of the important features of porous media is the presence of a large number of pores of various sizes; consequently, these media have large surface areas. A large number of pores facilitates separation and purification by means of filters and membranes[3,4]. Large surface areas make porous media suitable for the separation methods that rely on adsorption, such as chromatography[5], as well as catalytic reactions in fuel cells and batteries[6]. However, mass transfer through porous media in these processes is quite complicated because of the complexity of the pore structure. The bottlenecks and the tortuous pathways often observed in the porous media may inhibit the transport, which is known as the bottleneck effect. The fact common to the all the aforementioned processes is that the mass transfer characteristics, and consequently the performance, are greatly affected by the size and shape distribution of pores owing to the complexity and diversity of pore structure[7]. For the optimal design of a process of high efficiency and performance, the fundamental knowledge on mass transfer characteristics in porous media, particularly the effect of porous structure, is required. However, it has not been fully understood yet.

Mass transfer is generally attributed to convection and diffusion (or dispersion). These processes are very sensitive to pore geometry; therefore, it is extremely important to predict transport properties such as the local concentration of substances inside complicated porous channels. For example, the design of porous filters or catalysts is important for effective performance and should be determined on the basis of internal transport properties. In addition, transport properties become more intricate if the porous geometry changes as a result of chemical reactions with substances present in the system[8-10]. As shown in Figure 1, when a substance dispersed in fluid (black dots in Figure 1) reacts with the surface of a solid porous medium (assembly of gray round objects), the concentration field varies due to the consumption of the substance by the reaction as well as changes in the geometry of the medium are brought about by the reaction product (black deposits on the porous media). The changes in concentration and channel geometry affect the transfer of the substance and consequently the reactive flux. The reaction generates a

renewed concentration gradient and further changes the porous geometry, which affects mass transfer. Visualization and quantification of the variance of the concentration field from moment to moment is one of the most effective approaches for better understanding of such intricately continuous transport phenomena in porous media.

For the investigation of concentration (density) variance, optical visualization techniques such as the shadowgraph[11], schlieren[12], and Mach-Zehnder methods[13] have traditionally been employed. The shadowgraph and schlieren methods are based on the dependence of the refractive index on density, while the Mach-Zehnder method provides local concentration variances by recording the interference fringe[14]. However, these three methods require the use of complex and expensive experimental apparatus. Laser-induced fluorescence (LIF) enables the visualization of scalar distributions such as concentration, temperature, and pH by laser excitation of a fluorescent dye, whose emission intensity is dependent on the intended quantity[15]. Methods that involve the use of tracers, such as the LIF method, have the great advantage that the velocity and concentration fields can be measured at the same time if particle image velocimetry (PIV) is simultaneously employed[16]. While the use of tracers often simplifies measurement, tracer-free methods are required for the analysis of mass transfer in reactive or narrow channels since the presence of the tracers may affect the reactive surface area or the flow resistance, respectively. Light absorption photometry is based on the relationship between absorbance and medium concentration and represents one of the methods suitable for use in reactive or narrow channels. Although it has been commonly employed to measure the concentration of homogeneous solutions, light absorption photometry can be applied to the visualization of inhomogeneous two-dimensional concentration fields through the use of collimated light irradiation[17,18].

The reconstruction and quantification of the concentration field from the visualization images obtained by the above methods has been performed[19,20]. In particular, visualization by light absorption photometry is possible by the use of simple experimental apparatus; it is applicable to the quantification of concentration fields without any complicated additional equipment and only requires the preparation of a standard curve. Owing to the measurement principle of light absorption photometry, the concentration field is obtained in a non-destructive, non-invasive, and real-time manner. Furthermore,

the recent development of optical and image-capturing systems would enable increasingly accurate quantification due to increased resolution of images.

The present paper is aimed to intensively examine complicated changes in concentration fields using visualization and quantification based on light absorption photometry. We particularly focused on mass transfer at a porous edge, *i.e.*, at the entrance of porous media, in the direction of gravity. We consider a simple system where the substance is transferred downward in a liquid and is consumed at the porous edge by the reaction. In such a system, the distribution of substances in the porous medium is extremely uneven since the behavior of the substance depends not only on the surrounding concentration fields but also on the geometry of porous edge. From a practical point of view, the clogging of porous membranes during filtration processes is a common problem[21]. Once the edge of the membrane is clogged, substance behavior in the whole system is considerably altered, which seriously affects the total efficiency of the filtration process. Despite the importance of the mass transfer in the vicinity of a porous edge, there have been few studies undertaken in this area. The basic understanding of how substances in a fluid behave near the porous edge and how they invade into media with complicated geometries is therefore needed.

In terms of mass transfer near the edge of porous media, the present study has been performed for the following purposes: (1) development of a non-contact method for measurement of the concentration field near the entrance regions of reactive porous media and (2) investigation of the influence of porous edge geometry on invasion behavior according to the concentration field obtained by the measurement system designed in (1). In this study, we mainly intend to exhibit the fact that the mass transfer through porous media in the direction of the gravity is influenced by various factors. We show that the invasion behavior of substance into the porous media greatly depends on tiny unevenness of the inlet shape. It is markedly different from a well-known diffusion behavior caused by concentration gradient. There have been some studies on each phenomena focused here, i.e., the vertical mass transfer on supply and consumption systems[11], invasion of substance into porous media having

complex edge geometry[8], and change of flow channel geometry in porous media by deposits[9,10]. However, in most of realistic systems, these phenomena occur simultaneously. Therefore we want to show how these combined effect changes mass transfer into porous media by simple model experiments. The edge of the porous medium is modeled by an assembly of impermeable spherical particles, which is similar to the system used in our previous study[18]. To model the boundary condition (consumption of a substance for reaction) at solid surface, we have adopted electrochemical deposition, which allows the control of total boundary flux. Although the influence of the electric potential on the local reaction (deposition) rate cannot be neglected, it does not affect ion transfer in the electroneutral region as explained in later sections. The variance of the non-uniform concentration field from moment to moment and the scale of the unsteady convection flow caused by the concentration gradient are examined.

The outline of the present paper is as follows. In the first section, the experimental system and the methodology are exhibited. A detailed description of the influence of the electric field on mass transfer is also given in this section. In the second section, the theoretical analysis of Rayleigh-Taylor instability, which is caused by the concentration gradient in the direction opposite to gravity, is described. In the next section, we show a series of changes in the concentration field obtained from the experiments. The conclusions are presented at the end of the paper.

Experimental Methodology

Model of mass transfer near porous edges

The present study focuses on mass transfer in the vicinity of a porous edge under the influence of gravitational force. As shown in Figure 1, a substance supplied from above moves in a liquid toward the solid porous media located at the bottom of the system. The substance is partly consumed by a deposition reaction on the surface of the media, while the rest enters the media further through the void spaces.

To model such a phenomenon, an electrochemical deposition experiment is utilized so that the overall reaction rate can be controlled. Figure 2 shows a schematic representation of the experimental setup. As shown in Figure 2(a), we employed a quasi-two-dimensional vertical cell of length l = 10.0 mm, height h = 10.7 mm, and width w = 1.0 mm. The cell was filled with 1.0 M copper sulphate solution. As a model of porous media, a particulate bed made of stainless steel (diameter d_p = 1 mm) was placed at the bottom of the cell, while a flat copper plate was placed at the top. A constant current I = 10 mA was applied for one hour under galvanostatic conditions. The particulate bed and the copper plate function as the anode and cathode, respectively. The copper plate dissolves cupric ions into the solution, while the ions shift in reaction to the metallic copper deposits on the surface of the particulate bed. The experimental cell is similar to that utilized for the visualization of mass transfer in our previous study[18]. Since the deposition cell is oriented vertically, the transfer of ions from the copper plate to the particulate bed is affected by gravity. We measured the two-dimensional inhomogeneous concentration field of cupric ions during the experiment by the absorption technique described below.

With regard to the particulate bed, we adopted three arrangements, as shown in Figure 2(b). In all arrangements, the height and length of the beds were h_b = 3.7 mm and l_b = 9.5 mm, respectively. We expected that the invasion behaviors of ions into porous media greatly depend on the edge geometry. That is, the local flow rate of ion would vary drastically with a tiny difference of the outer shape of the media. The structures A, B, and C have a similar geometry but there are subtle differences of concavo-convex shape and interval between overhangs. The difference between structures A and B lies in the presence of a particle on the left side of the bed. Structure C consists of four particle overhangs, while structures A and B had three. They are adopted as simple examples to exhibit the effect of edge geometry on the ion invasion. By comparing the concentration fields formed in these structures, we investigated the dependence of ion transfer on complex solid surface geometry.

Despite the presence of the electric field, most of the electrolyte solution, except for the reacting boundary regions, exhibited electroneutrality, *i.e.*, the net charge was zero.

$$z_c c_c = z_a c_a \tag{1}$$

where z is the valence of the ion and c is the concentration. The subscripts c and a represent the cation and anion, respectively. Mass transfer under the electroneutral conditions can be apparently interpreted as a case of an advection-diffusion system without the electric field[22,23]. The cationic concentration can be described as follows:

$$\frac{\partial c_c}{\partial t} = D\nabla^2 c_c - \boldsymbol{v}\cdot\nabla c_c \tag{2}$$

where v is the fluid velocity vector. D represents the ambipolar diffusion coefficient given by

$$D = \frac{u_c D_a + u_a D_c}{u_c + u_a} \tag{3}$$

where u_c, u_a and D_c, D_a are the mobility and the diffusion coefficient of the cation and anion, respectively. The transfer of the anion can be considered in the same manner as the cation. At the reacting solid surface on the outside of the electroneutral region, the boundary flux (r_c) for the reaction (deposition and dissolution) can be described by the multiplication of the reaction rate per unit area (k_c) and the ion concentration at the electrode surfaces (c_c^s).

$$r_c = k_c c_c^s \tag{4}$$

Equation (4) is the same in form as the boundary flux in the non-electrolytic case, although the rate constant is only the one which is dependent on the electric potential as expressed below:

$$k_c = A_c \exp\left(-\frac{E_a^c + \alpha_c z_c F\left(E_{eq} + \eta\right)}{RT}\right) \tag{5}$$

where R is the gas constant, T is the absolute temperature, A_c is the frequency factor, E_a^c is the activation energy, α_c is the migration coefficient, F is the Faraday constant, and E_{eq} is the equilibrium potential. These parameters are given by the experimental conditions. η is the overpotential, which is determined by the position-dependent electric potential in the solution near the reacting boundary. In summary, ion transfer in the electroneutral region and the boundary flux can be described in the same form as for non-electrolytic systems, and only the reaction rate depends on the electric potential. In that sense, the system considered here is not purely an advection-diffusion system.

However, the spatial variance of the electric potential at the solid boundary would not affect ion transfer in most parts of the solution.

Measurement of the concentration field by light absorption technique

Figure 2 (c) shows the apparatus for concentration measurements. An observation object (the solution in a quasi-two-dimensional cell) was placed between the light source and a microscope fitted with a CCD camera. The gap length between collimator lens and cell, and that between infrared filter and cell are $l_{gl} \approx 10$ mm and $l_{gm} \approx 150$ mm, respectively. The light was collimated by the lens, which was mounted at the tip of an optical fiber connected to the light source. The cell was irradiated from behind during the experiment, and images of the cell were taken from the front.

The relation between the concentration of the solution and the intensity of the light passing through the solution is basically described by the Lambert-Beer law. When light with intensity I_0 passes through a solution in a vessel with width w [mm], the light intensity after absorption I_1 and the concentration of the solution c [M] are related as follows:

$$\log_{10} \frac{I_1}{I_0} = -\varepsilon c w \tag{6}$$

where ε [$mm^{-1}M^{-1}$] represents the molar extinction coefficient, which depends on experimental conditions such as the nature of the solution and light intensity.

In the present study, this technique was applied to the measurement of non-uniform concentration fields during the deposition experiment outlined above. We employed near infrared (NIR) light with a wavelength greater than 780 nm as the irradiation light because the cupric ion used in the deposition experiment has an absorption peak at around 810 nm[17]. Figure 3 shows the relationship between cupric ion concentration and NIR intensity in case of particulate structure C. For accuracy, a standard curve was prepared for every experiment. Solutions with higher concentrations appears to be darker (*i.e.*, lower light intensity) since the ion absorbs the NIR light, while at lower concentrations the solutions appear brighter since there are fewer ions to absorb the light. The light intensity observed in Figure 3 is proportional to the concentration (linear correlation

coefficient $r_c^2 = 0.996$). The molar extinction coefficient is obtained from the least squares method as $\varepsilon_c = 0.62$ mm^{-1}M^{-1}. The standard curves in particulate structures A and B also indicate a linear relationship between concentration and transmitted light intensity (correlation coefficients $r_a^2 = 0.991$, $r_b^2 = 0.996$); the molar extinction coefficients were $\varepsilon_a = 0.68$ mm^{-1}M^{-1} and $\varepsilon_b = 0.59$ mm^{-1}M^{-1}, respectively. The extinction coefficients are different for the structures because the installation of the optical system and the light intensity are slightly different in each experiment. However, it scarcely affects the measurement because every standard curve adequately indicates a linear relationship. The concentration fields in the cells are calculated by comparing the brightness of each pixel in the images taken during the experiments with the standard curves and the reference images taken prior to the experiments. In principle, this method enables the non-contact measurement of time-dependent changes in the two-dimensional concentration field of various objects provided that a light source of appropriate wavelength is selected.

Theoretical analysis of gravity-driven instability

As described in the previous section, we are concerned with mass transfer into porous media in a vertical direction driven by gravity. In our deposition experiment, the cupric ion was supplied at the top of the cell and was consumed by deposition onto the particulate bed at the bottom. In such a system, the density (concentration) gradient develops in the direction opposite to gravity. It is known that gravity-driven instability occurs if high density fluid is located above low density fluid (Rayleigh-Taylor instability). Consequently, it is expected that mass transfer is enhanced by convective flow resulting from the instability. Such a convective mass transfer due to density differences has been studied in many engineering and science fields[11,24-31]. In electrochemical systems, de Bruyn JR has observed the Rayleigh-Taylor instability in an electrolyte cell between horizontally aligned flat electrodes[11].

In general, Rayleigh-Taylor instability is observed at the interface of both miscible and immiscible fluids. In both cases, the dominant wavelength and the growth rate of instability can be calculated by linear stability analysis. Under the condition in which molecular diffusion is less

significant, the dominant wavelength of a miscible interface is asymptotically close to that of an immiscible interface with no interfacial tension[32]. In our experiments, the timescale of molecular diffusion is obviously much larger than that of convection, as shown below. Therefore, we performed a linear stability analysis of the Rayleigh-Taylor instability, which is expected in our experiment, assuming an immiscible interface with no interfacial tension. We calculated the lengthscale of the instability (dominant wavelength) between the upper dense region and the lower dilute region.

For simplicity, we consider two immiscible fluids having different physical properties. The fluctuations of density and velocity of these fluids in a quasi-two-dimensional cell can be described as the superposition of perturbations with different wavelengths, for example,

$$\rho(y) = \overline{\rho}(y) + \hat{\rho}(y)\exp(nt)\exp(ikx)\zeta(z) \tag{7}$$

where $\overline{\rho}(y)$ is the density of the upper or lower fluids and $\hat{\rho}(y)$ is the perturbation. *x*, *y*, and *z* is the lateral, vertical, and gap direction, respectively (see Figure 2 for the coordinate system). *k* is the wave number, *n* is the growth rate, and $\zeta(z) = 6/w^2\left(w^2/4 - z^2\right)$ is called the Poiseuille factor (*w* is cell width in *z* direction). Substituting Eq. (7) into Stokes equation, the dispersion relation in a quasi-two-dimensional cell is obtained as follows[30]

$$\begin{aligned} -\left[\frac{gk}{n^2}(\alpha_1 - \alpha_2) + \beta_1 + \beta_2\right]\left[\beta_1 q_1 + \beta_2 q_2 - k(\beta_1 + \beta_2)\right] - 4k\beta_1\beta_2 \\ + \frac{4k^2}{n}(\alpha_1\overline{\nu}_1 - \alpha_2\overline{\nu}_2)\left[\beta_1 q_1 - \beta_2 q_2 + k(\beta_1 - \beta_2)\right] \\ + \frac{4k^3}{n^2}(\alpha_1\overline{\nu}_1 - \alpha_2\overline{\nu}_2)^2(q_1 - k)(q_2 - k) = 0 \end{aligned} \tag{8}$$

where $\overline{\rho}_1$ and $\overline{\nu}_1$ are the density and kinetic viscosity ($\overline{\nu} = \overline{\mu}/\overline{\rho}$, $\overline{\mu}$: viscosity), respectively, of the lower dilute fluid, and $\overline{\rho}_2$ and $\overline{\nu}_2$ are the density and kinetic viscosity of the upper dense fluid, respectively. The other parameters are defined as $\alpha_1 = \overline{\rho}_1/(\overline{\rho}_1 + \overline{\rho}_2)$, $\alpha_2 = \overline{\rho}_2/(\overline{\rho}_1 + \overline{\rho}_2)$, $\beta_1 = \alpha_1\left(1 + \overline{\nu}_1\eta/n\right)$, $\beta_2 = \alpha_2\left(1 + \overline{\nu}_2\eta/n\right)$, $q_1 = \sqrt{n/\overline{\nu}_1 + k^2 + \eta}$, $q_2 = \sqrt{n/\overline{\nu}_2 + k^2 + \eta}$, and $\eta = -\partial^2\zeta/\partial z^2 = 12/w^2$. Eq. (8) describes the growth rate of perturbations having various wave

numbers.

Figure 4 indicates the relationship between the wave number k and the growth rate n, calculated using Eq. (8) for our experimental conditions. We set the densities to be $\bar{\rho}_1 = 1.12\times10^3$ kg/m^3 (1.0 M copper sulphate solution) and $\bar{\rho}_2 = 1.14\times10^3$ kg/m^3 (1.2 M copper sulphate solution), the viscosity to be the same as that of 25.0 °C water, and $\bar{\mu}_1 = \bar{\mu}_2 = 0.890$ mPa·s. As can be seen in Figure 4, the growth rate has a peak value with respect to the wave number. This indicates that a wave of a certain wave number becomes dominant, while the other waves decay as time proceeds. Figure 4 indicates that the dominant wave occurs at $k_{max} = 3.7$ mm^{-1}. From these results, it is expected that the lengthscale of the gravity-driven instability arising at the interface between higher and lower concentrations in our experimental cell is $\lambda_{max} = 2\pi/k_{max} = 1.7$ mm. In the following sections, we compare the theoretical wavelength derived here to the lengthscale of concentration variance obtained from the measurements.

Results and discussion

Observation of the concentration field

Figure 5 shows the time evolution of the concentration field during the electrochemical deposition experiments. In Figure 5, the black spheres are the stainless particulate beds onto whose surface the cupric ions are consumed for the deposition. The copper plate that supplies the ions to the solution is located above the image. The intermediate part is filled with the electrolytic solution and the color in the image represents the concentration of the cupric ions (see color legend) with isoconcentration lines at 0.01 M intervals. The x [mm] and y [mm] presented in each images in Figure 5 are the scale of the actual experimental cells and the directions correspond to the coordinate system shown in Figure 2.

At the onset of the experiment, (I) $t = 1$ s, the uniform concentration, $c = 1.0$ M, is detected in all structures, which is set as the initial condition of the experiment. After a few seconds, a non-uniform and complicated concentration field is observed (Figure 5 II, III, and IV). Because of the gravitational force, mass transfer in the present experiment is found to differ from the well-known advection-diffusion features, which would generate a vertically continuous concentration field. Instead, the lower and higher

concentration regions respectively migrate in a cluster. Our measurement system could capture such a complicated ion transfer by detecting the concentration fields that range in size from several tens of micrometers to several millimeters.

A detailed description about the mass transfer observed in Figure 5 is given below. The higher concentration fluid formed on the upper side of the cell moves downward as if it is immiscible with the surrounding fluid. Then a finger-like pattern is created by gravitational instability because the concentration gradient occurs in the direction opposite to gravity. For all structures, there are several fingers with a roughly even size at (II) $t = 9$ s and (III) $t = 12$ s in Figure 5.

As mentioned in the previous section, the characteristics of the finger-like instability (dominant wavelength and growth rate) are obtained from the linear stability analysis. In this case, the dominant wavelength of instability corresponds to the finger width (in lateral direction) at initial stage, while the growth rate of instability describes the exponential growth of fingers with time. In our experimental condition, the dominant wavelength calculated from Eq. (8) is $\lambda_{max} = 1.7$ mm. The finger width in the lateral (x) direction which is visually observed from images shown in Figure 5 is comparable with λ_{max} (See inset scale in Figure 5).

On the other hand, the lower concentration fluid emerges as a thin layer along the surface of the particulate bed as if it is also immiscible with the surrounding fluid. Because of the lower density, the fluid in the layer accumulates around the uppermost particles and then begins to flow upward. The flow is not similar to the finger-like downward flow, but shows highly local and streaky features. In other words, the gravity-driven flow generated on the indented surface of the particulate bed is more likely to climb up toward the uppermost particles than it is to form the finger-like flows across the whole reacting surface. These features of upward flow, i.e., the low concentration fluid forms thin layer and moves upward along the complicated solid surface, are quite unexpected.

Velocity of convection flow in the initial stage

Figure 6 shows the concentration variation along the y (vertical) direction for the particulate bed with structure B. The values of the concentrations are averaged in the x (horizontal) direction from $x = 1.00$

mm to 8.00 mm, and they are normalized by the bulk concentration c_b. In Figure 6, the upward and downward mass transfer in the system is clearly detected. As shown in Figure 5, high concentration clusters settle down from the upper part with roughly similar size and velocity. The size of these clusters (and consequently the settling velocity) is determined by the characteristics of the instability. On the other hand, Figure 5 also indicates that low concentration clusters flow up from the top of the particulate bed. In this case, the size of the clusters is obviously affected by the shape of porous edge since it is completely different from that of the high concentration clusters observed in the vicinity of the flat solid surface. From Figure 5, the rising velocities of the low concentration clusters seem to be similar to each other. The time course across Figure 6(a), (b), (c), and (d) indicates that, in average sense, the mass transfer from the upper flat surface is achieved by downward flow with high concentration and low velocity, while the mass transfer from the lower indented surface is achieved by upward flow with low concentration and high velocity.

The amounts of supplied and consumed cupric ions seem to be uneven in Figure 6 although they should be equal in terms of mass balance. This is because the concentration shown in Figure 6 is calculated in the ranges of 1.00 mm $\leq x \leq$ 8.00 mm and 0.00 mm $\leq y \leq$ 6.40 mm despite the presence of concentration variation outside these ranges.

The velocity of the downward flow is determined by the scale of gravity-driven instability. The velocity becomes larger as the fingers formed by the instability increase in size[31]. The lengthscale of the finger, which is affected by the container shape and the concentration of substances[31, 32], could be also calculated theoretically as described above. On the other hand, the velocity of the upward flow depended obviously on the geometry of porous edge and was therefore difficult to calculate. Note that the supplied and consumed substances in the present experiment have the same ion equivalents due to the nature of the electrochemical deposition experiment. In the case where the inlet rate of a substance and the rate of consumption due to precipitation are unequal, the transfer velocities observed would depend on each rate.

In Figure 6, concentration variations are approximated by a series of straight lines. The downward and upward flow is represented by sloping sections in which the concentration changes through space.

The midpoint between the starting and end points of each slope in the y direction are defined as the travel distance d_t; these are plotted against time in Figure 7. In the case of the upward flow, d_t is measured from the point of y = 6.40 mm. As shown in Figure 7, there is a great difference in the travel distances of the downward and upward flows. The mean velocity among structures A, B, and C, estimated by the least square method, is 0.22 mm/s for the downward flow and 0.97 mm/s for the upward flow.

Figure 7 shows no significant difference in the velocity of the downward flow among the structures since this convection flow is caused by the Rayleigh-Taylor instability. For the upward flow, the slope of the trend line is also similar for all structures, indicating that the flow velocity is almost independent of the structure once the low concentration fluid begins to float up. The travel distance in structure C is, however, smaller than the others, which suggests retardation of the upward flow in this structure. This is attributed to the number of particle overhangs present in the structure. As shown in Figure 5, the upward flow occurs after the accumulation of the low concentration fluid at the top of the uppermost particles. It is inferred that more time is taken in particulate structure C to accumulate the volume of lighter solution necessary to initiate flow at each overhang. The mass transfer near the indented solid surface is divided into two processes; migration of low concentration solution toward the top of particulate bed and generation of upward flow with low concentration. It is found from Figure 7 that, while the former process depends on the structure (the difference of intercept of lines in Figure7), the latter process is independent of the structures (same gradient of lines in Figure7). These two processes play significant roles on mass transfer in the vicinity of reacting surfaces, however, the former process is less important in the steady state. From the above results, it is found that a slight difference in porous edge geometry has considerable influence on the rate of mass transfer.

Variation of convection flow scale after a passage of time

Figure 8 shows the concentration profile in the x direction at y = 2.00 mm for structure B. The concentration is uniform at the onset of the experiment ((a) t = 1 s) and then undergoes a subtle fluctuation due to the influence of the upward flow ((b) t = 9 s). The fluctuation has a few local and

narrow peaks in Figure 8(b) since the upward flow is streaky and dependent on the geometry of the particulate bed. After a few seconds, the concentration increases overall, and the fluctuation in concentration displays a larger wavelength and amplitude ((c) t = 12 s). The increase in concentration arises from the presence of the more dense downward flow. The period of the dominant fluctuation in Figure 8(c) seems to be close to the theoretical wavelength λ_{max} = 1.7 mm. As time progresses, however, the fluctuation with an unexplained ambiguous wavelength appears, which is generated by complex interactions between the downward and upward convections ((d) t = 30 s).

The Fourier analysis was performed using the results in Figure 8 for the rough evaluation of the time variance in lengthscale of concentration fluctuation caused by the development of the convections. Figure 9 shows the spectrum of the concentration variation in the x direction at y = 2.00 mm. The results at t = 12 s is selected because the upward and downward flows have not interacted yet at this instant and therefore the lengthscale of the concentration variation should be consistent with the theoretical dominant wavelength λ_{max} of the Rayleigh-Taylor instability. As shown in Figure 9 for all structures, a large contribution of the concentration variation with wavelength close to λ_{max}, i.e., λ_a = 1.55 mm, λ_b = 1.88 mm, and λ_c = 1.88 mm, is observed at t = 12 s. However, the peak wavelength has obviously changed (into λ_a = 4.64 mm, λ_b = 4.71 mm, and λ_c = 1.34 mm) at t = 30 s where the downward finger-like flow and the upward streaky flow interact with each other. Since the convection flow, particularly the upward flow, is significantly affected by geometry as discussed above, it is inferred from Figure 9 that the lengthscale of the convection flow at t = 30 s is dependent on the geometry of the porous edge.

Figure 10(a) shows the time variation of the wavelength of the convection flow λ_{cv} which represents the peak wavelength. As mentioned above, the wavelength at t = 12 s peaks at around the theoretical dominant wavelength λ_{max} (dashed line in Figure 10a) for all structures since the downward finger-like flow has not been affected by the upward streaky flow yet. After that, these flows start to interact and it changes the peak values differently in structures A, B, and C. The lengthscale of the concentration variation in structure A gradually shifts into longer scale (λ_{cv} = 4.64 mm), which implies that the

convection flow with larger scale is generated. In structure B, short (λ_{cv} < 1.7 mm) and long (λ_{cv} = 4.71 mm) wavelengths are alternately detected as peak value. It is inferred that the concentration field consists of the large-scale variation by the convection flow and small-scale fluctuations. The lengthscale in structure C becomes shorter and it is settled in λ_{cv} = 1.34 mm.

Figure 10(b) shows the relation between the wavelength of the convection flow λ_{cv} at t = 12 s and t = 30 s and mean interparticle distance l_m. The mean interparticle distance indicates the entrance spacing in the porous media and it is defined as the average of horizontal separation length between the tips of overhangs (or the cell wall). As shown in Figure 10, the values of λ_{cv} at t = 30 (filled circles) are obviously different depending on the structure while λ_{cv} at t = 12 s (crosses) is similar to the dominant wavelength (dashed line). The wavelength of the convection flow at t = 30 s is longer than the mean interparticle distance l_m in all structures. l_m in structure C is shorter than that in the others because of the larger number of overhangs. The comparison of structures A, B, and C in Figure 10 reveals that the difference in l_m affects the peak wavelength. The results indicate that the lengthscale of the convection flow depends on the scale of the void space at the edge of the porous media. In addition, the lengthscale of both the void space and the convection flow causes highly selective supply of substances deep in the porous media. As shown in Figure 5(IV), the denser flow reaches the coves surrounded by the particle overhangs in structures A and B, whereas this invasion can be scarcely observed for structure C. From these results, the void space at the edges of porous media has a crucial influence on mass transfer, including formation of convection flows and invasion of substances.

Deposition behavior of copper on the particulate bed

The growth of copper deposits on particulate beds is briefly described. Figure 11 shows particulate beds at the beginning (t = 0 min) and end (t = 60 min) of the experiments. As can be seen in Figure 11, the deposition is not uniform and it occurs selectively at the entrance to particulate beds. It should be noted that the change in the geometry of particulate beds in the present experimental system is merely a boundary condition of ion transfer. The influence of the electric potential on the deposition behavior cannot be neglected since the potential possibly affects the local reaction (deposition) rate (although it

does not affect ion transfer in the electroneutral region) as described in Eqs. (4) and (5). Nevertheless, Eq. (4) also indicates the dependence of the reaction rate on the concentration of the reactant at the reacting surface. The concentration at the surface seems to vary under the influence of the neighboring concentration field, which can be described in the same manner as non-electrolytic systems, as mentioned previously. In the present case, the concentration field surrounding the particulate bed is found to be greatly dependent on the convection flow from the bulk region toward the entrance of the bed. These results suggest that the inhomogeneous concentration field caused by the interaction between the upward and downward convection flows may affect the deposition behavior.

Conclusions

In the present paper, we have implemented a method based on light absorption photometry for the non-invasive measurement of two-dimensional concentration fields. This method has been applied to a quantitative evaluation of the mass transfer at the edge of porous media. As a result, the variance of a non-uniform complicated concentration field from moment to moment is appropriately captured with a spatial resolution of several tens of micrometers to millimeters. As well as non-contact processing, light absorption photometry offers great advantages, including simple apparatus and applicability to a wide range of objects by using a light source of appropriate wavelength.

The concentration field evaluated in the present study has a gradient in the direction opposite to gravity due to the precipitation and dissolution reactions. By using the experimental results, the non-steady convection flows caused by the gravity-driven instability have been analyzed in detail. It was found that the indented reaction surface generated local and streaky convection flows depending on the surface geometry, while a finger-like flow appeared in the vicinity of the flat surface. After the passage of time, the flows interact closely with each other and generate a more complicated convection flow with a new lengthscale. The convection flow and the geometry of the porous edge could result in a highly selective supply of substances deep in the media. The results quantitatively reveal that the geometry of a porous edge considerably affects mass transfer, such as the lengthscale and velocity of convection flow and the invasion of substances into media.

Literature cited

1. Wiesner MR, Grant MC, Hutchins SR. Reduced permeability in groundwater remediation systems: role of mobilized colloids and injected chemicals. *Environ. Sci. Tech.* 1996;30:3184-3191.
2. Johnson A, Patil S, Dandekar A. Experimental investigation of gas-water relative permeability for gas-hydrate-bearing sediments from the Mount Elbert Gas Hydrate Stratigraphic Test Alaska North Slope. *Mar. Petrol. Geol.* 2011;28:419-426.
3. Zhang LZ. A Lattice Boltzmann simulation of mass transport through composite membrane. *AIChE J.* 2014;60:3925-3938.
4. Sun SP, Chung TS, Lu KJ, Chan SY. Enhancement of flux and solvent stability of Matrimid thin-film composite membrane for organic solvent nanofiltration. *AIChE J.* 2014;60:3623-3633.
5. Basconi JE, Carta G, Shirts MR. Multiscale modeling of protein adsorption and transport in macroporous and polymer-grafted ion exchangers. *AIChE J.* 2014;60:3888-3901.
6. Holzer L, Wiedenmann D, Münch B, Keller L, Prestat M, Gasser Ph, Robertson I, Grobéty B. The influence of constrictivity on the effective transport properties of porous layers in electrolysis and fuel cells. *J. Mater. Sci.* 2013;48:2934-2952.
7. Gaiselmann G, Neumann M, Schmidt V, Pecho O, Hocker T, Holzer L. Quantitative relationship between microstructure and effective transport properties based on virtual materials testing. *AIChE J.* 2014;60:1983-1999.
8 Li X, Huang H, Meakin P. Level set simulation of coupled advection-diffusion and pore structure evolution due to mineral precipitation in porous media. *Water Resour. Res.* 2008;44:W12407.
9. Colón CFJ, Oelkers EH, Schott J. Experimental investigation of the effect of dissolution on sandstone permeability, porosity, and reactive surface area. *Geochim. Cosmochim. Acta*

2004;68:805-817.

10. Sallès J, Thovert JF, Adler PM. Deposition in porous media and clogging. *Chem. Eng. Sci.* 1993;48:2839-2858.
11. Bruyn JR. Fingering instability of gravity currents in thin-layer electrochemical deposition. *Phys. Rev. Lett.* 1995; 74:4843-4846.
12. Marshall G, Mocskos E, González G, Dengra S, Molina FV, Iemmi C. Stable, quasi-stable and unstable physicochemical hydrodynamic flow in thins-layer cell electrodeposition. *Electrochimica. Acta* 2006;51:3058-3065.
13. Léger C, Elezgaray J, Argoul F. Experimental demonstration of diffusion-limited dynamics in electrodeposition. *Phys. Rev. Lett.* 1997;78:5010-5013.
14. Merzkirch W. *Flow Visualization 2nd ed*. Academic Press, 1987.
15. Kinsey JL. Laser-induced fluorescence. *Ann. Rev. Phys. Chem.* 1977;28:349-372.
16. Mizuta K, Odo Y, Yoshimitsu S, Kaji H, Murakami M, Matsumoto T. Transient behavior during a gas dissolution process around a stationary single bubble. *J. Chem. Eng. Jpn* 2008;41:553-556.
17. Rosso M, Chazalviel JN, Fleury V, Chassaing E. Experimental evidence for gravity induced motion in the vicinity of ramified electrodeposits. *Electrochim. Acta* 1994;39:507-515.
18. Otomo R, Ishii N, Takahashi K, Harada S. Mass transfer caused by gravitational instability at reactive solid-liquid interfaces. *J. Vis.* 2014;17:49-57.
19. Pasumarthi KS, Agrawal AK. Schlieren measurements and analysis of concentration field in self-excited helium jets. *Phys. Fluids* 2003;15:3683-3692.
20. Srivastava A, Muralidhar K, Panigrahi PK. Reconstruction of the concentration field around a growing KDP crystal with schlieren tomography. Appl. Optics 2005;44:5381-5392.
21. Innocentini MDM, Rodrigues VP, Romano RCO, Pileggi RG, Silva GMC, Coury JR. Permeability optimization and performance evaluation of hot aerosol filters made using foam incorporated alumina suspension. J. Hazard. Mater. 2009;162;212-221.

22. Newman J, Thomas-Alyea KE. *Electrochemical Systems 3rd ed.* New York: John Wiley & Sons, 2004.

23. Nicoli M, Castro M, Cuerno R. Unified moving-boundary model with fluctuations for unstable diffusive growth. *Phys. Rev. E* 2008;78:021601.

24. Pedley TJ, Kessler JO. Hydrodynaimc phenomena in suspension of swimming microorganisms. *Annu. Rev. Fluid Mech.* 1992;24:313–358.

25. Hoyal DCJD, Bursik MI, Atkinson JF. Settling-driven convection: A mechanism of sedimentation from stratified fluids. *J. Geophys. Res.* 1999;104:7953–7966.

26. Völtz C, Pesch W, Rehberg I. Rayleigh–Taylor instability in a sedimenting suspension. *Phys. Rev. E* 2001;65:011404-1–7.

27. Riaz A, Hesse M, Tchelepi HA, Orr FM JR. Onset of convection in a gravitationally unstable diffusive boundary layer in porous media. *J. Fluid Mech.* 2006;548:87–111.

28. Ennis-King J, Paterson L. Coupling of geochemical reactions and convective mixing in the long-term geological storage of carbon dioxide. *Int. J. Greenh. Gas Control* 2007;1:86-93.

29. Burns P, Meiburg E. Sediment-laden fresh water above salt water: linear stability analysis. *J. Fluid Mech.* 2012;691:279–314.

30. Harada S, Mitsui T, Sato K. Particle-like and fluid-like settling of a stratified suspension. *Eur. Phys. J. E* 2012;35:1-6.

31. Harada S, Kondo M, Watanabe K, Shiotani T, Sato K. Collective settling of fine particles in a narrow channel with arbitrary cross section. *Chem. Eng. Sci.* 2013;93:307–312.

32. Fernandez J, Kurowski P, Limat L, Petitjeans P. Wavelength selection of fingering instability inside Hele-Shaw cells. *Phys. Fluids* 2001;13:3120-3125.

Figure Captions

Fig.1 Mass transfer with precipitation reaction at the entrance of porous media: (a) A fluid (white part) with a substance (black dots) moves in the direction of arrows into porous media

(assembly of gray round objects). (b) After the passage of time, the geometry of the medium changes owing to the reaction product (black deposits on the porous media) and it varies the transport of the substance.

Fig. 2 Schematic representation of the experimental setup: (a) electrochemical deposition cell, (b) three different particulate structures, (c) measurement apparatus.

Fig. 3 Standard curve and images of copper sulfate solutions obtained prior to the deposition experiment in particulate structure C.

Fig. 4 Relationship between wave number k and growth rate n in this experiment.

Fig. 5 Concentration fields of cupric ions at the initial stage in deposition experiments: (I) t = 1 s, (II) t = 9 s, (III) t = 12 s, (IV) t = 30 s.

Fig. 6 Mean concentration in the x direction which ranges from 1.00 mm to 8.00 mm at each position of y using the particulate structure B. They are normalized by the bulk concentration c_b.

Fig. 7 Travel distances of downward and upward flows in the initial stage.

Fig. 8 Concentration profile in the x direction at y = 2.00 mm in the particulate structure B.

Fig. 9 Spectrum of concentration variance in x direction at y = 2.00 mm.

Fig. 10 Relation between wavelength of convection flow λ_{cv} and mean interparticle distance l_m.

Fig. 11 Change in geometry of particulate beds at t = 0 min and t = 60 min as a result of deposition experiment.

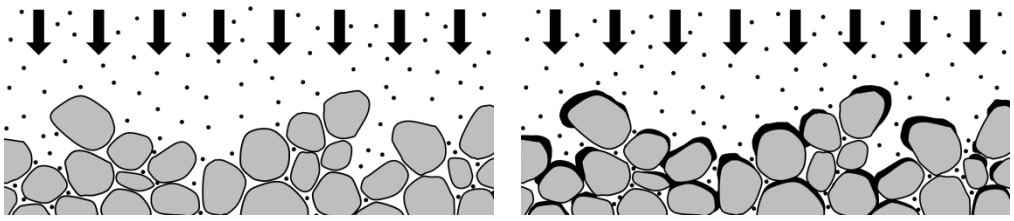

(a) (b)

Fig. 1 Mass transfer with precipitation reaction at the entrance of porous media: (a) A fluid (white part) with a substance (black dots) moves in the direction of arrows into porous media (assembly of gray round objects). (b) After the passage of time, the geometry of the medium changes owing to the reaction product (black deposits on the porous media) and it varies the transport of the substance.

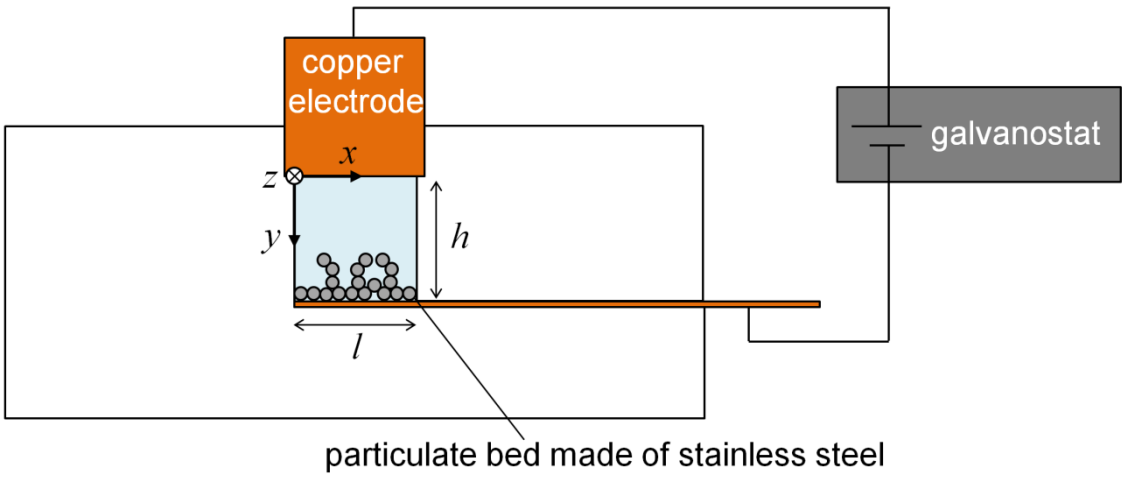

(a)

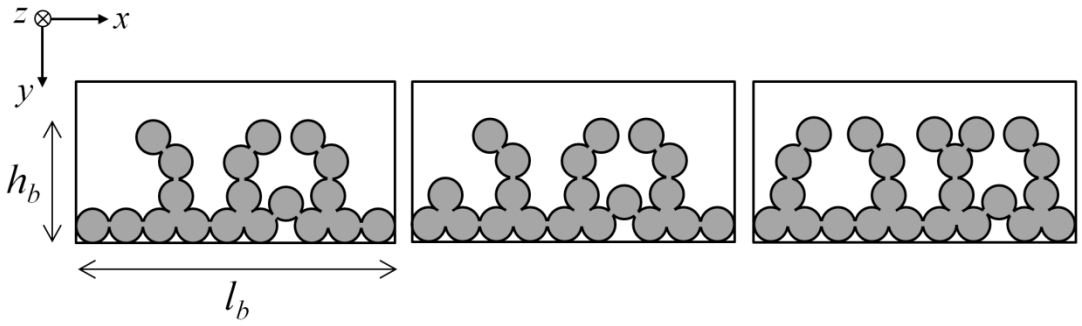

structure A structure B structure C

(b)

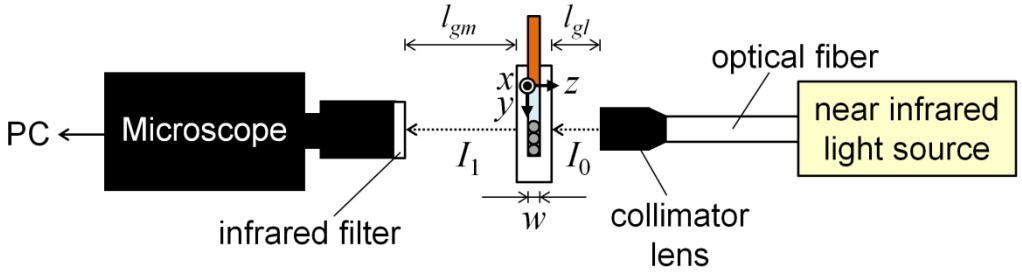

(c)

Fig. 2 Schematic representation of the experimental setup: (a) electrochemical deposition cell, (b) three different particulate structures, (c) measurement apparatus.

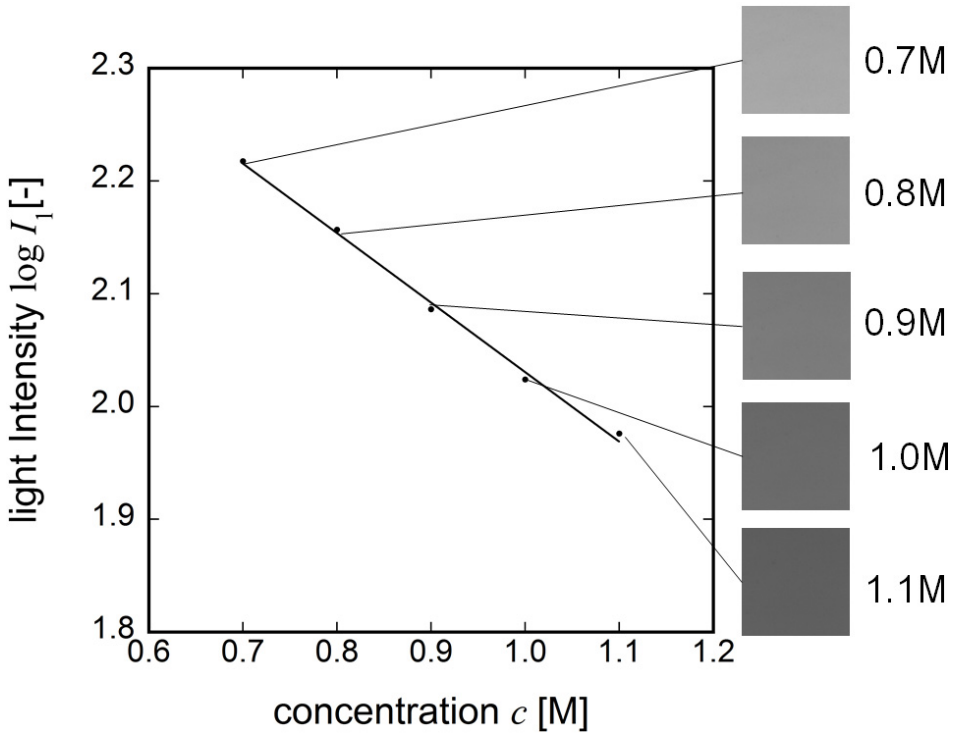

Fig. 3 Standard curve and images of copper sulfate solutions obtained prior to the deposition experiment in particulate structure C.

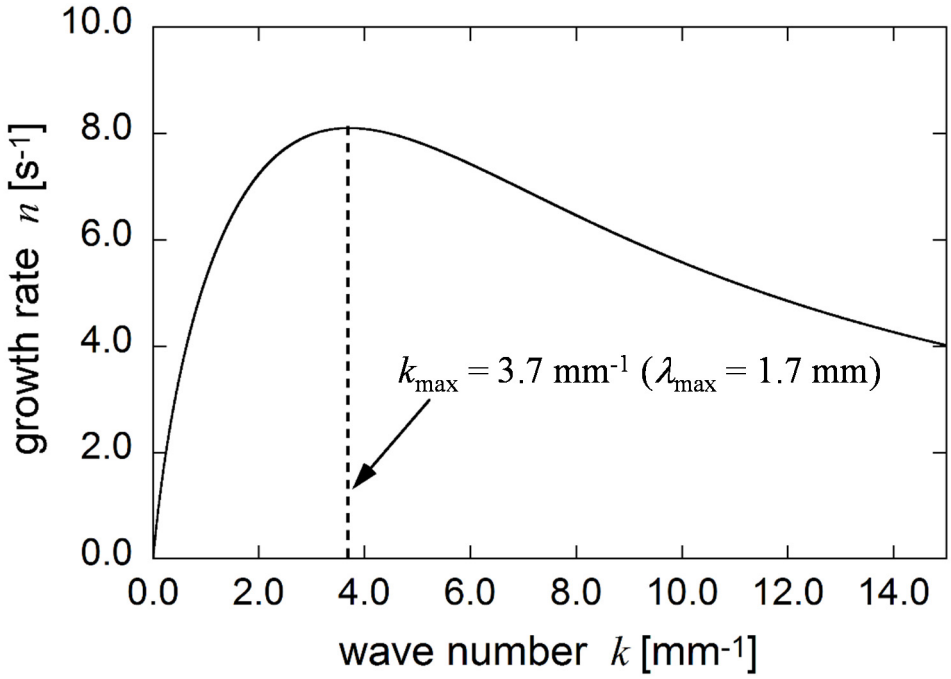

Fig. 4 Relationship between wave number k and growth rate n in this experiment.

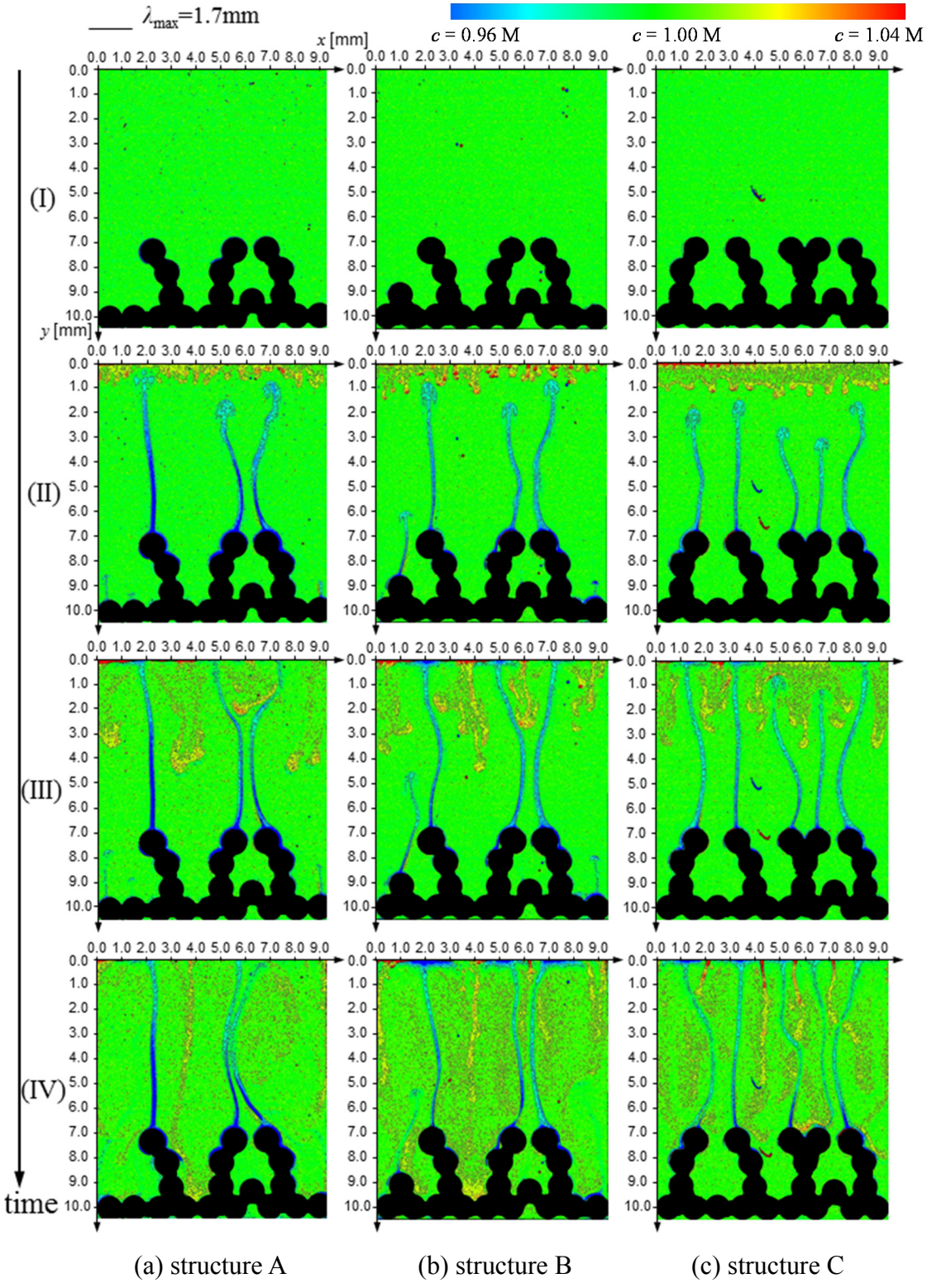

Fig.5 Concentration fields of cupric ions at the initial stage in deposition experiments: (I) t = 1 s, (II) t = 9 s, (III) t = 12 s, (IV) t = 30 s.

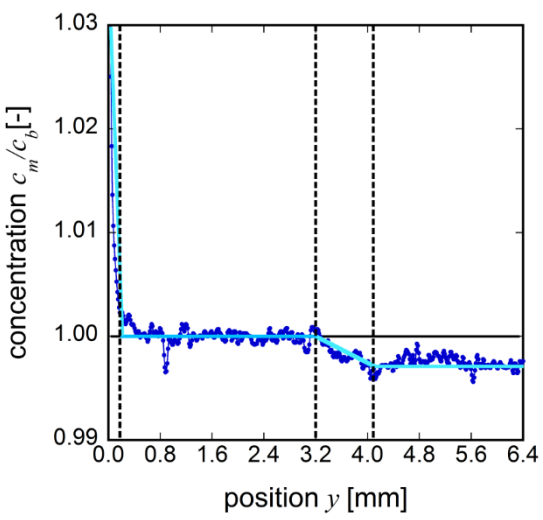

(a) t = 6s

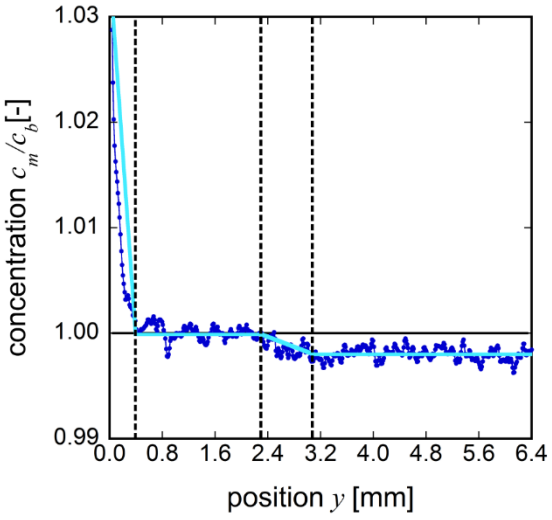

(b) t = 7 s

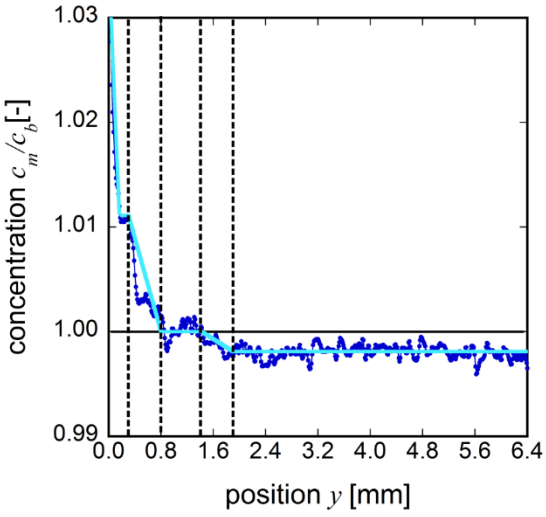

(c) t = 8 s

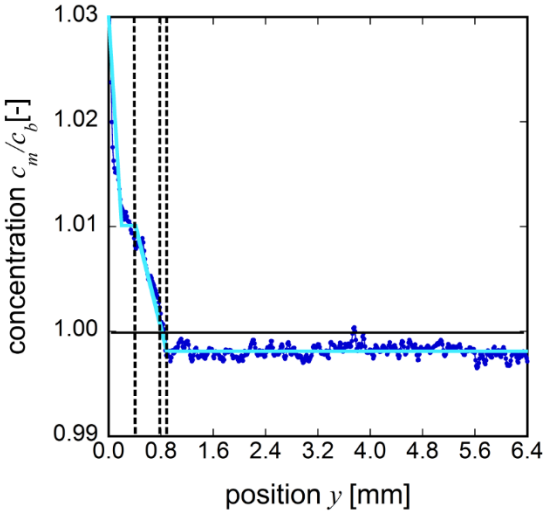

(d) t = 9 s

Fig. 6 Mean concentration in the x direction which ranges from 1.00 mm to 8.00 mm at each position of y using the particulate structure B. They are normalized by the bulk concentration c_b.

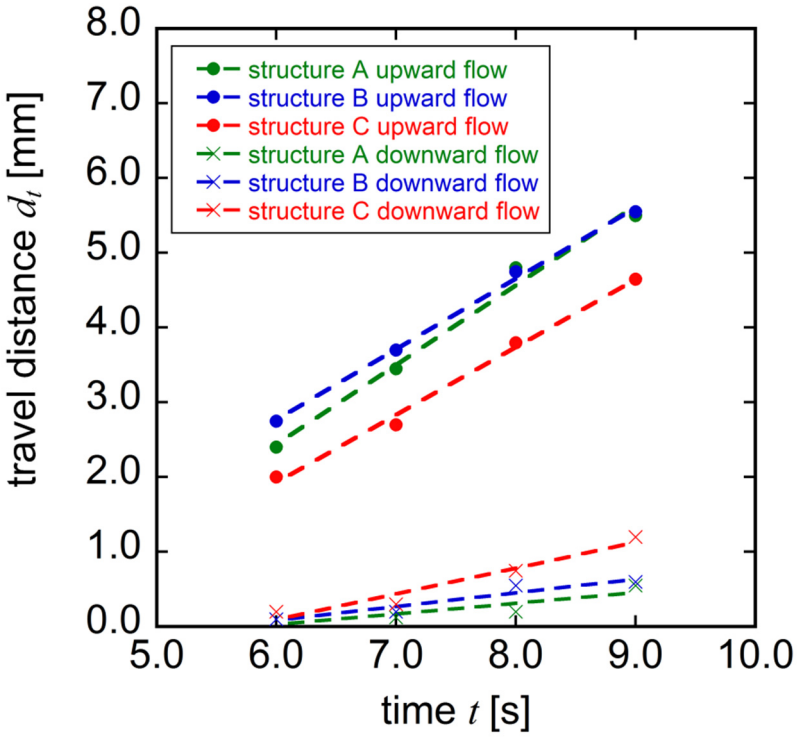

Fig. 7 Travel distances of downward and upward flows in the initial stage.

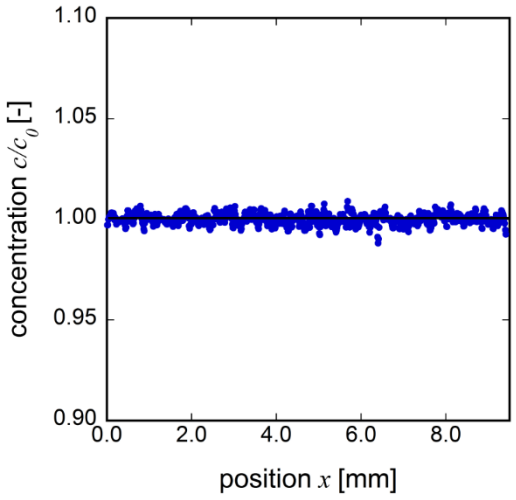

(a) t = 1 s

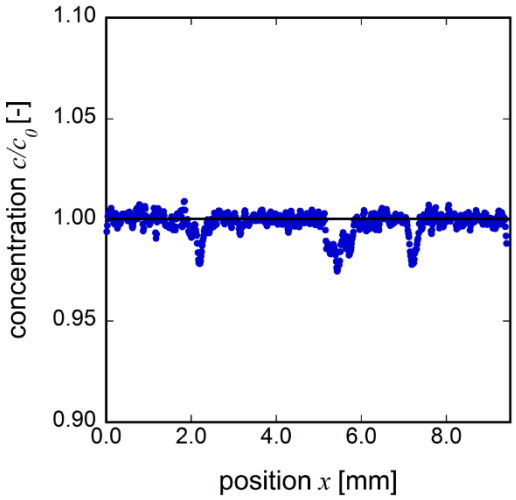

(b) t = 9 s

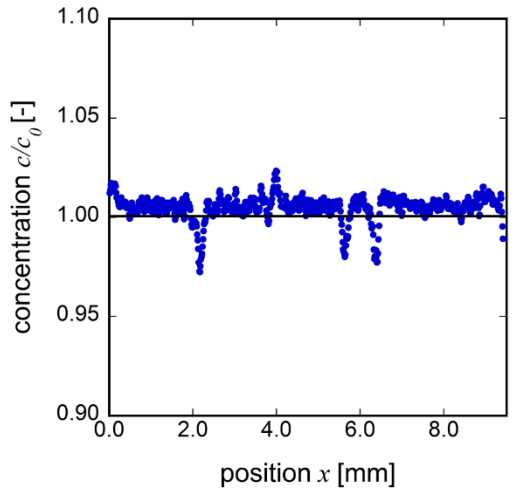

(c) t = 12 s

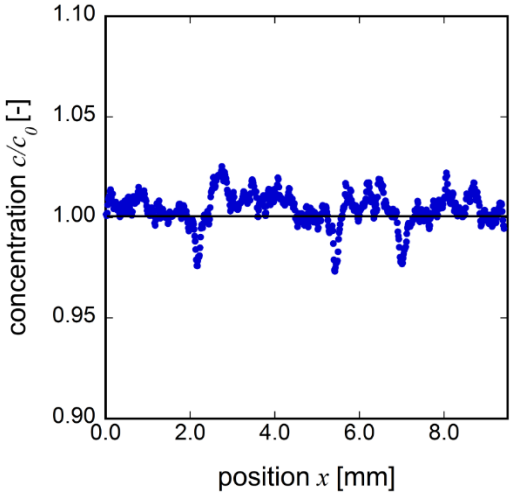

(d) t = 30 s

Fig. 8 Concentration profile in the x direction at y = 2.00 mm in the particulate structure B.

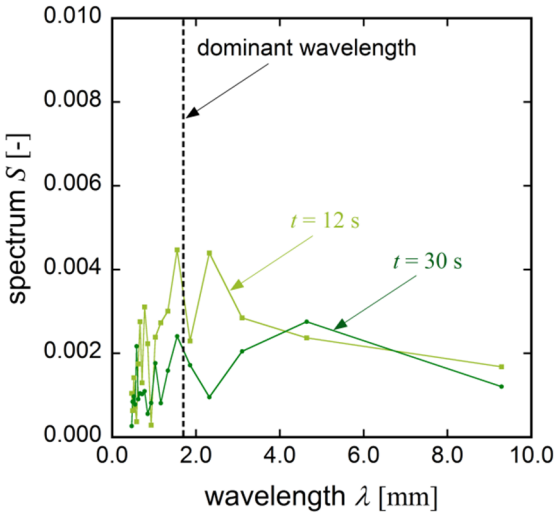

(a) structure A

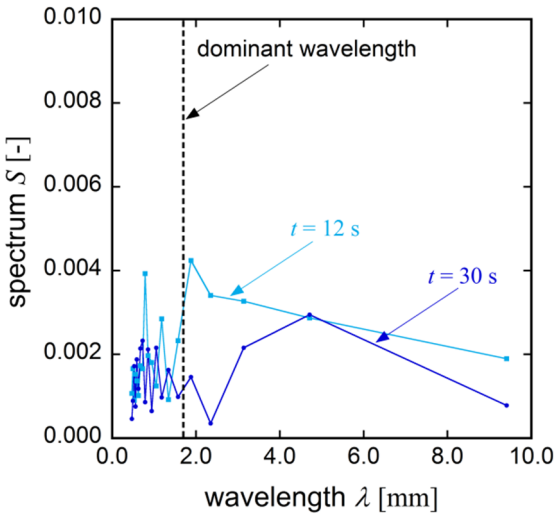

(b) structure B

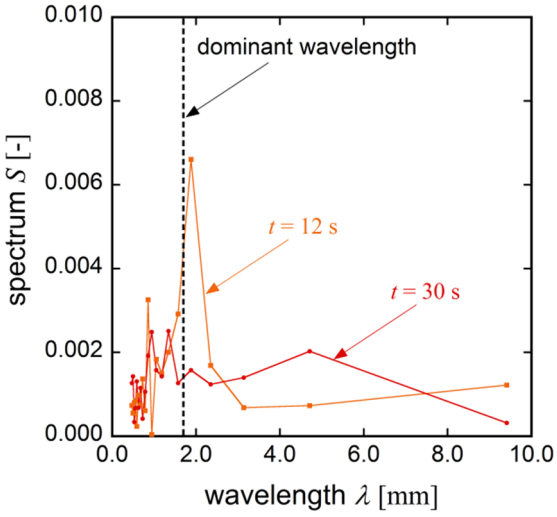

(c) structure C

Fig. 9 Spectrum of concentration variance in x direction at y = 2.00 mm

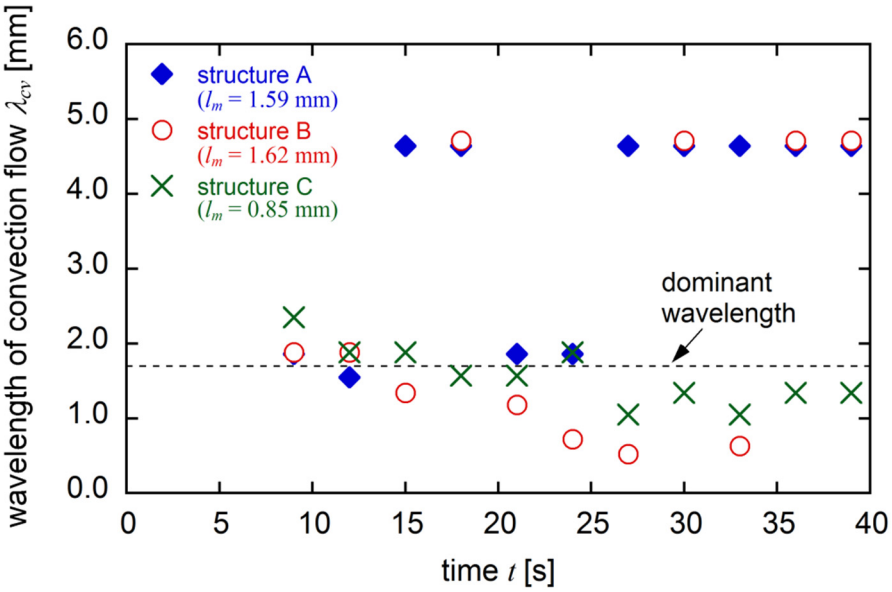

(a) Time variation of λ_{cv}.

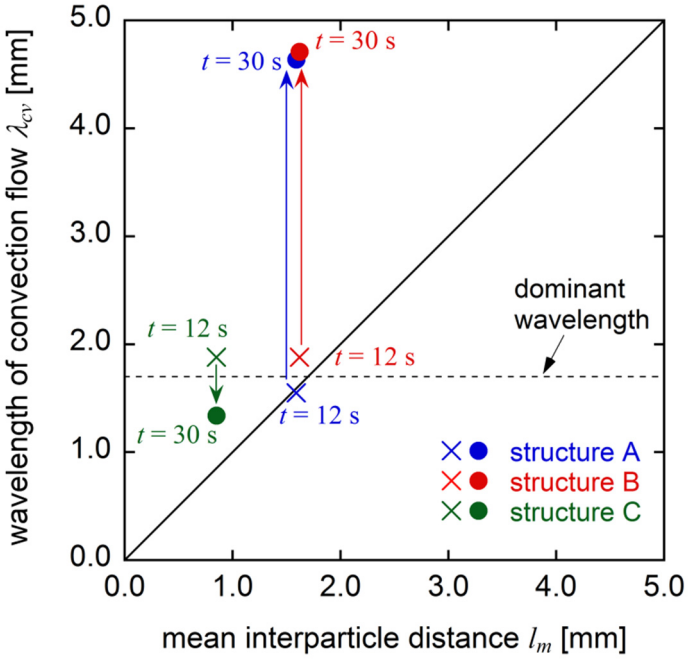

(b) Relation between λ_{cv} and l_m at t = 12 s and t = 30 s.

Fig. 10 Relation between wavelength of convection flow λ_{cv} and mean interparticle distance l_m.

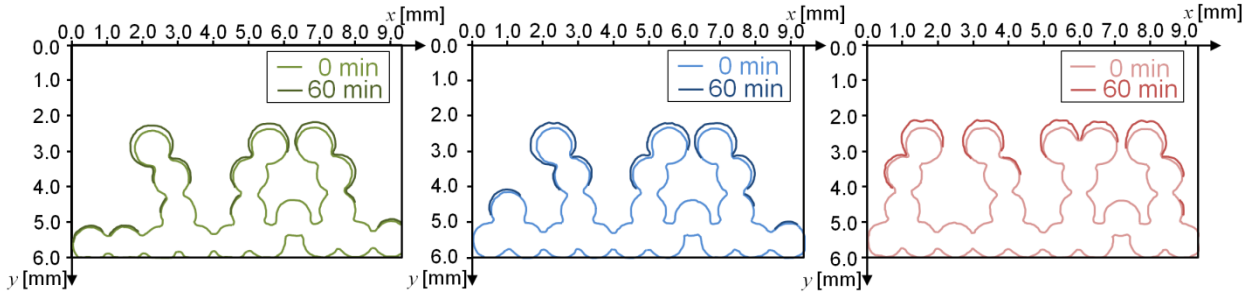

(a) structure A (b) structure B (c) structure C

Fig. 11 Change in geometry of particulate beds at $t = 0$ min and $t = 60$ min as a result of deposition experiment.